GEOPHYSICS®

IMPROVING ESTIMATES OF BURIED PIPE DIAMETER AND INFILLING MATERIAL FROM GPR PROFILES WITH FULL WAVEFORM INVERSION USING PEST

Journal:	*Geophysics*
Manuscript ID	GEO-2017-0617.R1
Manuscript Type:	Technical Paper
Date Submitted by the Author:	n/a
Complete List of Authors:	Jazayeri, Sajad; University of South Florida, School of Geosciences Klotzsche, Anja; Forschungszentrum Juelich, Agrosphere Kruse, Sarah; University of South Florida, School of Geosciences
Keywords:	ground-penetrating radar (GPR), full-waveform inversion, wavelet, deconvolution, high-resolution
Area of Expertise:	Engineering and Environmental Geophysics, Ground-Penetrating Radar

IMPROVING ESTIMATES OF BURIED PIPE DIAMETER AND INFILLING MATERIAL FROM GPR PROFILES WITH FULL WAVEFORM INVERSION

Authors:

Sajad Jazayeri, University of South Florida, School of Geosciences, Tampa, Florida, USA, email: sjazayeri@mail.usf.edu

Anja Klotzsche, Agrosphere (IBG-3), Institute of Bio- and Geosciences, Forschungszentrum Jülich, Jülich, Germany, email: a.klotzsche@fz-juelich.de

Sarah Kruse, University of South Florida, School of Geosciences, Tampa, Florida, USA, email: skruse@usf.edu

Original paper date of submission: November, 20, 2016

Revised paper date of submission: September 14, 2017

ABSTRACT

Ground penetrating radar (GPR) is a widely used tool for the detection and location of buried utilities. Buried pipes generate characteristic diffraction hyperbolas in raw GPR data. Current methods for analyzing the shapes and timing of the diffraction hyperbolas are very effective for locating pipes, but less effective for determining the diameter of the pipes, particularly when the pipes are smaller than the radar wavelengths, typically a few tens of cms. A full-waveform inversion (FWI) method is described for improving estimates of the diameter of a pipe and confirming the infilling material (air/water/etc.) for the simple case of an isolated diffraction hyperbola on a profile run perpendicular to a pipe with antennas in broadside mode (parallel to the pipe). The technique described here can improve a good initial guess of pipe diameter (within 30-50% of the true value) to a better estimate (less than ~8% misfit). This method is developed by combining two freely available software packages with a deconvolution method for GPR effective source wavelet (SW) estimation. The FWI process is run with the PEST algorithm (Model-Independent Parameter Estimation and Uncertainty Analysis). PEST iteratively calls the gprMax software package for forward modeling of the GPR signal as the model for pipe and surrounding soil is refined.

INTRODUCTION

Modern life depends on subsurface pipelines used to carry water, oil, gas, sewage and other fluids. Civil engineering and construction industries face the challenge of maintaining and repairing existing pipelines as well as laying new pipes. Increasing demand for new buried utilities increases the risk of damaging existing utilities (Lester and Bernold, 2007). As infrastructure ages, demand for repairs and replacement require knowledge of the locations and connectivities of multiple utility systems installed at different times, using different materials, in increasingly dense

networks, where records are often incomplete. In such scenarios, simply detecting a pipe at a given location may not be sufficient information. GPR resolution of not only the presence of the pipe, but the pipe diameter, pipe material, or pipe-filling material (e.g. air, water) could be a way to distinguish and map different generations or types of utilities.

GPR has become one of the primary tools of choice for mapping the locations of pipes in urban settings. The transmitting antenna emits an electromagnetic (EM) pulse that propagates into the subsurface. The EM pulse travels through the subsurface material and is reflected, scattered and attenuated. The reflection or scattering occurs when the pulse encounters a subsurface inhomogeneity, in particular soil heterogeneities or targets with contrasting dielectric properties (permittivity). (We note that the permittivity here is expressed as relative permittivity, which is the ratio of the material permittivity to the permittivity of free space.) The pulse attenuation is primarily controlled by the electrical conductivity of the soil. Reflected energy is recorded by the receiving antenna. The signal recorded at the receiving antenna contains a combination of the energy traveling in air and along the ground surface, reflected and refracted energy from soil inhomogeneities, buried targets (in this case pipes), and noise. A buried pipe generates a characteristic diffraction hyperbola because of its shape and contrast in electromagnetic properties with the background soil. The diffraction hyperbolas of pipes in GPR profiles are sufficiently distinctive that they can be displayed and interpreted in real time; hence GPR is widely used for on-the-spot utility detection.

GPR responses expected from underground utilities, drums, tanks, and cables have been described in the literature. Early modeling by Zeng et al. (1997) describes responses for a variety of utility scenarios, with air-filled, water-filled, and partially saturated pipes. Maierhofer et al.

(2010) provide a workflow for the typical common-offset GPR data analysis procedures as well as modelling and imaging techniques common to rebar detection. Benedetto and Pajewski (2015) describe examples of GPR surveys in civil engineering, including pavements, bridges, tunnels and buildings, underground utilities, and voids.

The horizontal position of an underground pipe on a GPR profile is readily established as the location of the peak of the characteristic diffraction hyperbola (Figure 1). Inferring the depth to the top of the pipe requires knowledge of the average velocity structure of materials over the pipe. Loeffler and Bano (2004) study the impact of water content on the permittivity and therefore on GPR signals by simulations of cylindrical objects in vadose zone. One way to derive the propagation velocity in the medium is by conducting a common-midpoint (CMP) or a wide angle reflection and refraction (WARR) survey, in which the spacing between transmitter and receiver is progressively increased. Following methods derived for stacking seismic data, layer velocities can be determined by semblance analysis (Fisher et al., 1992; Grandjean et al., 2000; Liu et al., 2014 and Liu and Sato 2014). This method has the advantage of recovering information on how velocity varies with depth, but it requires surveys with systems that permit variable offset between transmitter and receiver. Urban surveys require shielded antennas (to avoid reflections from surficial objects); most shielded systems cover a transmitter-receiver pair in a single shielded unit that does not lend itself to easy acquisition of CMP surveys. Alternatively, an average velocity can be determined from the shape and timing of the diffraction hyperbola that forms the GPR return from the pipe itself. So generally the pipe depth is estimated by finding the average velocity that best fits the measured hyperbola. However, Sham et al. (2016) observe that the curve-fitting method is biased by human judgment. Grandjean et al. (2000), Booth et al. (2011) and Murray et

al. (2007) describe the accuracy with which velocities, and hence depths of utilities, can be determined via both methods.

In this paper, we focus on how to extract additional information about pipes, beyond position and depth, from GPR profiles. Pipe diameter affects GPR returns, most visibly when the radar wavelength is small compared to the pipe diameter and the pipe's permittivity significantly different from surrounding soil (Roberts and Daniels 1996). In this case, distinct returns can be captured from the top and the bottom of the pipe, as shown in Figure 1 (e.g. Zeng and McMechan, 1997). It is easier to capture the dimensions of water-filled pipes than air-filled pipes because the slow radar velocity in water delays the return from the bottom of the pipe by a factor of ~9 over the equivalent air delay. In either case, when the pipe is narrow enough that the top and bottom returns overlap and interfere, extracting information on pipe diameter from the single hyperbola is challenging. Wiwatrojanagul et al. (2017) reports no significant difference for the hyperbolic reflections for different rebar diameters. Diameter estimation based on fitting hyperbolas is clearly impacted by decisions about the phase of the pipe return selected for the fit (as one can choose either positive or negative phases, see Dou et al. 2017) and tradeoffs made in wave velocity and pipe diameter selections. The hyperbola-fitting method also cannot provide any information about the pipe-filling material.

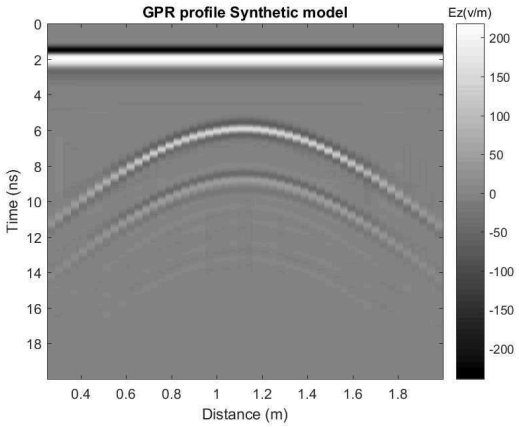

Figure 1. A synthetic GPR profile for an air-filled PVC pipe. The inner diameter of the pipe is 40 cm with wall thickness of 3 mm; the central frequency of antenna is 800 MHz. In this case distinct reflections from top and bottom of pipe are observed; later weaker arrivals are multiples.

Ristic et al. (2009) present a method to estimate both the radius of a cylindrical object and the wave propagation velocity from GPR data simultaneously based on the hyperbola fitting. In their method, the target radius is estimated by extracting the location of the apex of the hyperbola and the soil velocity that best fits the data for a point reflector, followed by finding an optimal soil velocity and target radius, using a nonlinear least squares fitting procedure. This method is handicapped because both variability in the GPR source wavelet and local complexities in the soil's permittivity and conductivity structure affect the shape of the returned pulse. This in turn affects how the arrival times of diffracted returns are defined. These perturbations to the arrival time can be on the order of the changes expected with changing cylinder diameter, making it difficult to distinguish pipe diameter from wavelet from permittivity and conductivity complexities.

Other researchers have also investigated complexities associated with pipe returns. For example, GPR can be applied for leakage detection from the pipes. Crocco et al. (2009) and

Demirci et al. (2012) successfully detected water leakage from plastic pipes using GPR by applying microwave tomographic inversion and a back-projection algorithm, respectively. Ni et al. (2010) use a discrete wavelet transform (DWT) to filter and enhance GPR raw data in order to improve image quality. They find DWT to be advantageous in detection of deeper pipes if shallower anomalies obscure the reflected signal from deeper targets, but do not attempt to extract pipe diameter information. Janning et al. (2014) present an approach for hyperbola recognition and pipe localization in radargrams, which uses an iterative directed shape-based clustering algorithm to recognize hyperbolas and identifies groups of hyperbola reflections that belong to a single buried pipe.

Full-waveform inversion can potentially provide high-resolution subsurface images because it uses information from the entire waveform. If achieved, FWI can improve on estimates of pipe diameter made from ray-based arrival time analysis, as in Ristic et al. (2009). Virieux and Operto (2009) provide an overview of the development of this technique for seismic data. FWI on GPR data is most commonly applied on crosshole GPR data to study aquifer material (e.g. Ernst et al., 2007; Klotzsche et al. 2010, 2012, 2013 and 2014; Meles et al., 2010, 2012; Yang et al., 2013; van der Kruk et al., 2015; Gueting et al., 2015 and 2017 and Keskinen et al., 2017) or on frequency-domain air-launched GPR signals for a limited number of model parameters (Lambot et al., 2004, Tran et al., 2014, Mahmoudzadeh Ardakani et al., 2016, De Coster et al., 2016 and Andre et al., 2015). Lavoue et al. (2014) used frequency domain FWI to image 2D subsurface electrical structures on multi-offset GPR data. Kalogeropoulos et al. (2011) used FWI on surface GPR data to monitor chloride and moisture content in media. Busch et al. (2012) and Busch and van der Kruk (2014) applied FWI on surface GPR data to characterize

soil structure and to obtain conductivity and permittivity estimations. Busch et al. (2013) further applied FWI on surface GPR data to estimate hydraulic properties of a layered subsurface.

The method described in this paper builds on the previous work by applying the FWI method to the problem of pipe diameter and infilling material estimation. Multiple variables that influence the GPR diffraction hyperbola can be incorporated into the inversion process. Here, the method is assessed when the SW, average soil permittivity, pipe depth and horizontal position, pipe inner diameter, and pipe-filling material are optimized in the inversion. The method in its current state is only effective with diffraction(s) from one pipe, and does not yet share the advantages of the Ni et al. (2010) and Janning et al. (2014) methods that can distinguish multiple pipes.

We note that we are considering only an exceptionally simple case that provides a starting point for more thorough investigations. We only consider transects run perpendicular to a horizontal pipe with antennas in broadside mode (maintained parallel to the pipe and perpendicular to the transect). Polarizations effects on surveys oblique to pipes will be quite different (e.g. Villela and Romo, 2013).

METHOD

The method presented here for determining a best-fitting pipe diameter and other parameters involves five main steps (Figure 2): (1) basic processing of the raw GPR data; (2) defining the starting model using the ray-based diffraction hyperbola analysis; (3) transformation of 3D data to 2D; (4) finding a good effective SW; and (5) an iterative inversion process that runs to a threshold criteria to find the pipe diameter that best fits the data. The starting model created

in step (2) is defined using ray-based analysis of the data, whereby the average soil velocity and therefore electrical permittivity, soil electrical conductivity, pipe lateral location and depth are estimated. In this workflow the user must assume a permittivity of the pipe-filling material (for example a value expected for air, water, or sewage) and the pipe material (for example PVC) and pipe wall thickness. With these assumptions, a value for the electrical conductivity within the pipe and a starting estimate of the pipe diameter are also derived.

The inversion procedure in step (5) requires forward modeling of GPR wave propagation. Since forward modeling of 3D waves is computationally expensive, 2D forward modelling is used. This requires a 3D to 2D transformation on the data, accounting for the expected differences between the real source and a line source, and correcting the geometrical spreading factor.

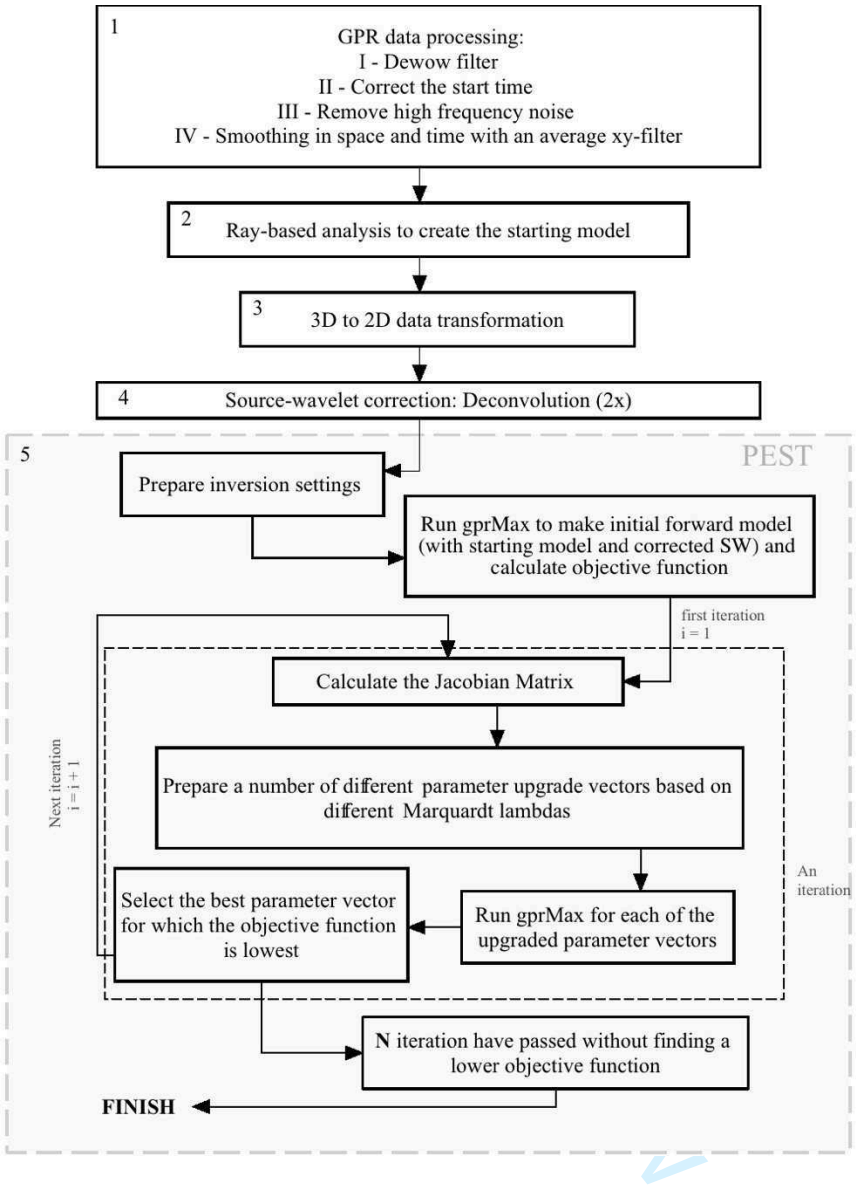

Figure 2. The inversion process flowchart. The critical steps prior to the PEST full waveform inversion (gray box) are (1) simple GPR data processing; (2) ray-based analysis to estimate the initial model; (3) 3D to 2D transformation; (4) source-wavelet correction(s) and (5) creation of a reasonably good initial model using the ray-based results and the estimated SW; starting the inversion.

We note that the goals of the method described here are to improve the initial estimates of pipe diameter and pipe-filling material and soil permittivity. Estimating the conductivity of the

pipe-filling material (or soil) would require further computational expense, in the form of updating the SW estimation (step (4)) at each iteration of the inversion process in step (5). Here, the conductivity values are estimated from ray theory and then fixed during the inversion process. To eliminate errors caused by inaccurate conductivity values, traces are individually normalized before misfit calculations in the inversion process. The pipe wall thickness estimate is also fixed in the inversion process, as typical values of a few-mm put it below the GPR signal resolution.

(1) Basic processing of raw GPR data.

Some initial processing of the GPR data is essential for the inversion process to work (see Figure 2, step 1). A standard dewow filter and time-zero corrections (e.g. Cassidy, 2009) are followed by a high-cut frequency filter (2 GHz for examples in this paper). High-frequency noise removal is important because the forward models generated during the inversion process (described below, Figure 3) simulate "clean" data without such noise. In practice, additional data smoothing in both the x and y (space and time) dimensions are found to help the inversion efficiency. The optimal window size for the xy filter appears to vary with individual data sets, and selection depends on the interpreter's experience. The combined effects of these processing steps on the signal amplitude, for all data presented here, is on average less than 1% through the traces. On the two noisiest traces, average amplitude change is 4%. The data are not gained.

(2) Defining the starting model using ray-based diffraction hyperbola analysis.

The FWI and the effective SW estimation are impossible without a good initial model. We use ray-based analysis to estimate the initial parameters (Figure 2, step 2). First, travel times of the peak amplitudes of the diffraction hyperbola (from the top of pipe, if two are observed) are

identified. Second, Radzevicius (2015)'s least squares method is then used to estimate the average soil velocity, pipe depth and lateral position that best fits the peak amplitude times, assuming the pipe to be a point diffractor and zero offset between antennas. If two distinct hyperbolas from the pipe top and pipe bottom are recognized, then the diameter d is estimated from the RMS average of the travel time differences Δt for the peak amplitudes of returns from pipe top and pipe bottom on traces in the diffraction hyperbola, where $d = \frac{v_{filling}}{2}\Delta t_{RMS}$ and $v_{filling}$ is the velocity assumed for the pipe-filling material. The interpreter can assume the pipe to be water- or air-filled to estimate $v_{filling}$. If the resulting diameter appears unreasonable, an alternative filling medium can be considered. (For most engineering utility scenarios, if distinct reflections from top and bottom of the pipe are recorded with 800 MHz antennas, it is likely that the pipes are water-filled.). For instance, a 10-cm diameter water-filled pipe generates almost the same time interval between the hyperbolas off the pipe top and pipe bottom as a 90-cm diameter air-filled pipe.) If no hyperbola from the pipe bottom can be recognized, the interpreter must rely on their best guess for the initial diameter based on knowledge of the site.

An average soil conductivity is estimated by a least squares approach described in Appendix A. The maximum absolute amplitudes on the recorded hyperbola from the top of the pipe are used to find the best conductivity model that fits the data.

With isolated, clear diffraction hyperbolas and some knowledge about the expected target properties, it is possible to make sufficiently good starting models that the inversion can proceed successfully. Meles et al. (2012) indicate successful inversion requires initial models return synthetic data pulses that are offset less than one-half wavelength from the measured traces. Ray-based analysis is critical for satisfying this criteria.

(3) 3D to 2D transformation

To simulate 2D line-source generated waveforms that would be equivalent to those observed in the 3D data, a transformation is applied to the data (see Figure 2 step 3). This transformation is a prerequisite for the application of the 2D forward modeling in the inversion process, as noted for example by Ernst et al. (2007), Klotzsche et al. (2010; 2013), and Meles et al. (2012). We follow the method developed by Forbriger et al. (2014) to transform 3D shallow seismic data to 2D. Their method convolves data in the time domain with a $\sqrt{t^{-1}}$ where t is travel time, followed by an amplitude correction. The convolution provides a $\pi/4$ phase shift and corrects the geometrical spreading difference between two and three dimensions.

(4) Source wavelet estimation

The effective SW needs to be estimated once data are transformed to 2D (Figure 2 step 4). The shape and the amplitude of the SW depend on the instrument used, ground coupling, and thee surficial soil permittivity and conductivity structure. As such the user has little control over the wavelet form while collecting data. However, a good effective SW estimation is critical to the success of the inversion. (Inversion runs without the wavelet estimation step yield markedly poorer results or fail to converge.) Ernst et al. (2007) and Klotzsche et al. (2010) proposed a deconvolution approach to correct an initial estimate of an effective SW, for crosshole GPR data. An improved SW is obtained by deconvolving radar data with the impulse response of the earth in the area of investigation (Ernst et al., 2007; Klotzsche et al., 2010; Kalogeropoulos et al., 2011). We adapt this deconvolution approach for the use of common-offset data. The deconvolution is applied with the ray-based model and the observed data to correct the SW, and the process is then

repeated a second time to yield a second corrected SW. Details of the procedure are described in Klotzsche et al. (2010).

The method requires an initial guess of the waveform. For the instrument and terrain conditions in the case studies presented here (a Mala Geosciences ProEx 800 MHz shielded antenna on partially saturated clean sands) we find that the fourth-derivative of a Gaussian wavelet (second derivative of a Ricker wavelet) is effective. The efficiency of the FWI method is found to be highly dependent on the availability of an accurately corrected SW. The recovered SW is in turn dependent on the starting model (impulse response) of soil and pipe properties, and on the number of data traces and time window within traces used in the wavelet correction. Errors in the starting model propagate into the effective SW, and errors in the amplitude of the SW in particular can trade off with errors in the conductivity model.

Since the conductivity estimations in the FWI approach are highly dependent on the SW, a successful FWI analysis that aims to estimate the conductivity values requires the SW to be updated at each iteration of the FWI process. Busch et al. (2012; 2014) extended the deconvolution approach for surface WARR GPR data and combined it with a frequency-domain FWI for a horizontally layered media that better describes the sensitivity of the SW estimation to subsurface parameters. Thereby, Busch et al. (2012; 2014) combined the FWI and an effective SW update in terms of medium parameters and wavelet phase and amplitude. In contrast to common-offset data, WARR data provide more information about amplitude decay with changing offset and allow a better conductivity estimation. Adapting this approach to common-offset data is beyond the scope of this paper, and we thus expect errors associated with both the SW amplitude estimation and the conductivities in the inversion process. We recognize this limitation in the method by eliminating

soil conductivity as an inversion parameter (it remains fixed at the initial value), and reducing the impact of the soil conductivity on the inversion process by normalizing traces individually when calculating the cost (objective) functions at each inversion step.

(5) Full-waveform inversion

As the fifth and final step, the GPR returns from the pipe are inverted in order to improve on the initial model of soil and pipe. In this paper, the inversion procedure is designed using two software packages that are freely available. The first, the PEST (Model-Independent Parameter Estimation and Uncertainty Analysis) package (http://www.pesthomepage.org) is used for inverting the data to find the best model parameters (Doherty, 2015). The second, gprMax 2D (Giannopoulos, 2005; Warren et al., 2016) is used to compute the GPR readings expected at each step as the model parameters are updated (Jazayeri and Kruse, 2016). Because small cell sizes are necessary for the inversion to accurately recover the pipe dimensions, a 3D forward model, although clearly preferable, was too computationally expensive for this study.

PEST, prepared by John Doherty and released in 1994, is a package developed for groundwater and surface water studies (http://www.pesthomepage.org), but can be linked to any forward modeling problem. PEST uses the Gauss-Marquardt-Levenberg nonlinear estimation method (Doherty, 2010; 2015).

The relationship between the model parameters (e.g. pipe radius, soil permittivity, etc.) and the model-generated observation data (GPR returns) is represented by the model function M, which maps the n-dimensional parameter space into m-dimensional space, where m is the number of observational data points d. M should be differentiable with respect to all model parameters

(Doherty, 2010). A set of parameters, P_0 thus generate the model observations d_0 (equation 1). While generating another set of data d from a P vector slightly different from P_0, the Taylor expansion provides equation 2 as an approximation, where J is the M's Jacobian matrix.

$$d_0 = M(P_0) \quad (1)$$

$$d = d_0 + J(P - P_0) \quad (2)$$

The best fitting model is that which produces the minimum of the cost function φ (equation 3), where d is the real data collected and Q is an $m \times m$ diagonal weights matrix.

$$\varphi = \left(d - d_0 - J(P - P_0)\right)^t Q \left(d - d_0 - J(P - P_0)\right) \quad (3)$$

If u is denoted as the parameter upgrade vector, $u = P - P_0$, it can be written as:

$$u = (J^t Q J)^{-1} J^t Q R \quad (4)$$

where R is the non-normalized vector of residuals for the parameter set, $R = d - d_0$.

This approach needs to be given a set of starting model parameters (P_0), which will be updated in order to find the global minimum of the cost function (φ) in the time domain. The optimization process can benefit from adjusting Eq. 4 by adding a Marquardt parameter (α). The new form of the upgrade vector can be rewritten as equation 5, where I is the $n \times n$ identity matrix.

$$u = (J^t Q J + \alpha I)^{-1} J^t Q R \quad (5)$$

For problems with parameters with greatly different magnitudes, terms in the Jacobian matrix can be vastly different in magnitude. The roundoff errors associated with this issue can be

eliminated through the use of an $n \times n$ diagonal scaling matrix S. The ith element of the scaling matrix is defined as:

$$S_{ii} = (J^t Q J)_{ii}^{-1/2} \qquad (6)$$

Finally, Eq. 6 can be rewritten as:

$$S^{-1}u = ((JS)^t Q JS + \alpha S^t S)^{-1} (JS)^t Q R \qquad (7)$$

The largest element of $\alpha S^t S$ is often denoted as the Marquardt Lambda (λ), and can be specified to help control the parameter upgrade vector u and optimize the upgrade process.

To start the inversion PEST makes an initial call to gprMax to compute the initial GPR dataset expected from the starting model P_0 with the corrected SW (Figure 2, step 5). The Marquardt λ value is set to 20 and PEST computes the initial cost function φ. Then, a lower λ value is set and the cost function recalculated. This process is repeated until a minimum cost function is found. If a lower cost function is not observed by λ reduction, a higher lambda will be tested. Parameters P are then updated using the λ value that yields the minimum cost function, and the next iterations starts, with gprMax called again from PEST to compute the new corresponding GPR readings d_0. PEST then computes the residuals R between the updated model and real data. The next iteration starts with the best Marquardt λ from the previous iteration. If, in the next iteration, a lower cost function is not achieved, a new vector of updated parameters will nevertheless be tested. This process continues until the step at which a lower cost function is not found after N iterations. The N in this process was set to 6. The user can also specify upper and lower bounds for the parameters P. In this study, the relative permittivity is restricted between 1 and 90 and pipe diameters are bounded between 0 and 20 cm.

A concern in any inversion process is that the algorithm leads to a local minimum rather than the global minimum solution. For the real data, we cannot unambiguously identify the global minimum. To avoid local minima trapping we follow, to the extent possible, the recommendation described above that the initial synthetic data set is offset less than one-half wavelength from the measured data (e.g. Meles et al., 2012; Klotzsche et al., 2014). To then qualitatively assess the likelihood that our results presented represent a local minima, we run the inversion process with multiple sets of initial model parameters P_0, and compute the cost function φ at the conclusion of each run. The selection of initial models is described below. Runs that terminate with variable best-fit parameters P and differing cost functions φ are suggestive of termination at local minima.

RESULTS AND DISCUSSION

Synthetic model

This inversion method is evaluated by creating a 3D synthetic model of a PVC pipe filled with fresh water and buried 35 cm in homogenous semi-dry sand (Figure 3, left; Table 1). The model is used to generate synthetic 3D GPR readings. The GPR dataset (Figure 3, right) is created assuming a common-offset survey with an 800 MHz antenna set with 14 cm spacing between transmitter and receiver. Every 5 cm a pulse is transmitted and received, with 12 traces in total. The synthetic waveform is a 4th derivative of the Gaussian waveform, similar to those of some commercial systems (Figure 3, center). The cell size in the gprMax 3D forward model is 1 mm by 1 mm by 1 mm.

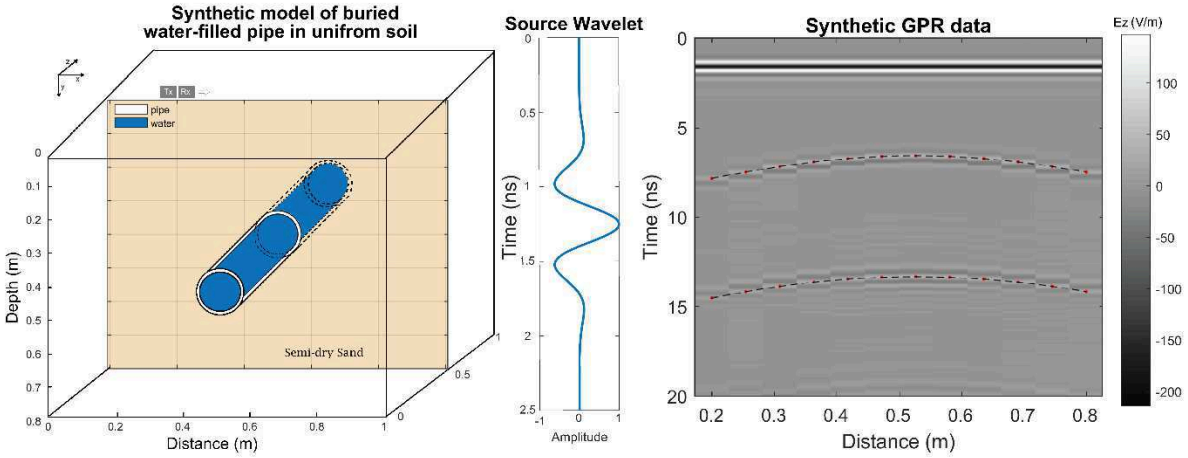

Figure 3. Left. Model geometry for a PVC pipe containing fresh water embedded in semi-dry sand. Pipe inner and outer diameter are 10 and 10.6 cm, respectively. The colored cross sections shows the part of the model over which the antenna has moved. Middle, the 800 MHz 4th derivative Gaussian wavelet assumed for the GPR signal. Right, the GPR profile produced by synthesizing readings every 5 cm across the model. Red dots show the arrival time picks used in the ray-based inversion. Black dashed lines show the arrival time curves predicted form the ray-based inversion parameters.

The ray-based analysis is applied to the synthetic GPR data (Figure 3, right) assuming the pipe to be water-filled. The ray-based analysis estimates the diameter with 15% error (Table 1). In contrast, an air-filling assumption results in ~1030% error in diameter estimation. Lateral position and soil average permittivity and conductivity are well estimated using the ray-based analysis (Table 1). The 3D to 2D transformation is applied, and the transformed data are then treated as the 'observed data' in the inversion process.

A uniform soil permittivity, a uniform effective soil conductivity, a uniform effective in-filling conductivity, and the pipe lateral position and depth are set following the methods described

above. Therefore, the unknown parameters in the inversion process are defined to be uniform soil and pipe-filling permittivities, pipe depth and inner diameter. In this scenario, the pipe is assumed to be known to be constructed of PVC of typical wall thickness (3 mm), and the pipe permittivity and conductivity are set to values appropriate for PVC (see Table 1). To mimic the inversion process in which the SW is not known, an initial guess of a Ricker wavelet is applied as the SW (Figure 4) and a synthetic 2D model is generated using the ray-based estimated model and the Ricker wavelet. For the wavelet estimation the direct air and ground wave are excluded. With the deconvolution method, the model SW is corrected (see Figure 4, first corrected SW). The synthetic data is again calculated with the first corrected wavelet. At the last step of the SW correction, the wavelet is deconvolved again using the second synthetic data and the observed data (e.g. Klotzsche et al., 2010). In this process, the symmetric Ricker shape wavelet is altered to a non-symmetric form closer to the real wavelet.

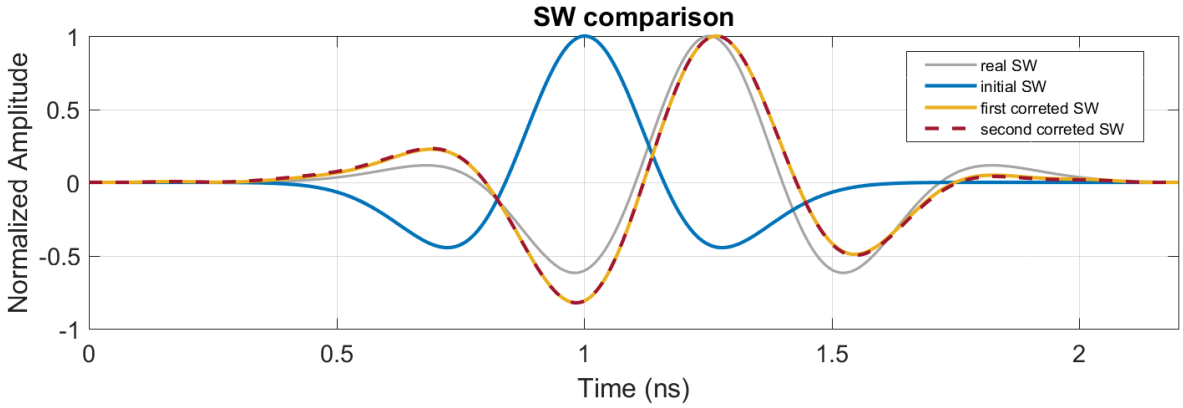

Figure 4. The real SW used to create 3D model (gray), initial SW used in the synthetic model (blue); the first (orange), and second corrected effective SW pulse (dashed red). Amplitudes are normalized.

Since the ray-based results are good approximations of the 'true' model parameters, Figure 5 illustrates that the effective SW correction alone produces a good fit between the hyperbola from the top of the pipe of the observed and modeled GPR traces. The inversion procedure for the soil and pipe properties and dimensions then brings improved alignment of the bottom of pipe diffraction returns (Figure 5), and reduces errors (Table 1). For instance, the ray theory estimated the pipe inner diameter to be 11.5 cm while the FWI process improved this estimate model parameter to 10.12 cm (1.2% error). The estimated depth also shows an improvement after the FWI process.

To study the effect of the initial value selection on the FWI results, the FWI process was run 22 times for this case, in each case varying the permittivity of pipe filling material and pipe diameter as initial model parameters. In each case the effective SW is computed with the model medium properties. The initial values were specified in 15 cases by randomly varying values in a Gaussian distribution around the best fit inversion results of Table 1 with a standard deviation of 50% of the ray-based result; and then in 7 cases by randomly assigning more extreme outliers to selected parameters. (A comprehensive examination of all 5 inversion parameters was computationally not feasible and is out of scope of this paper.) Figure 6 summarizes the changes in cost function from the initial value to the final inversion value for all runs, for pipe inner diameter (top) and pipe-filling relative permittivity (bottom). Note that only the first and last step of the inversion process are shown as the tail and tip of the arrows, the successive changes in parameters through multiple iterations are not shown.

Figure 6 (top) shows the diameter estimates are improved for all starting values within a factor of two of the true value. Many initial models converge at a 1-2 mm overestimate of the pipe

diameter, but the ray-based analysis starting model yields a final diameter only 0.12 mm greater than the true value, a difference less than the 1 mm cell size in the forward models. From Figure 6 (bottom), it can be concluded that inversions starting with significantly lower initial assigned in-filling relative permittivity values (<50) and initial pipe diameters that differed from the true diameter by more than 50% failed to reach within 10% of the true value. Lower initial pipe-filling relative permittivities (<=50) also significantly increased the time for convergence. We defer more detailed discussion of starting models to the more realistic field case studies described below.

Table 1, here

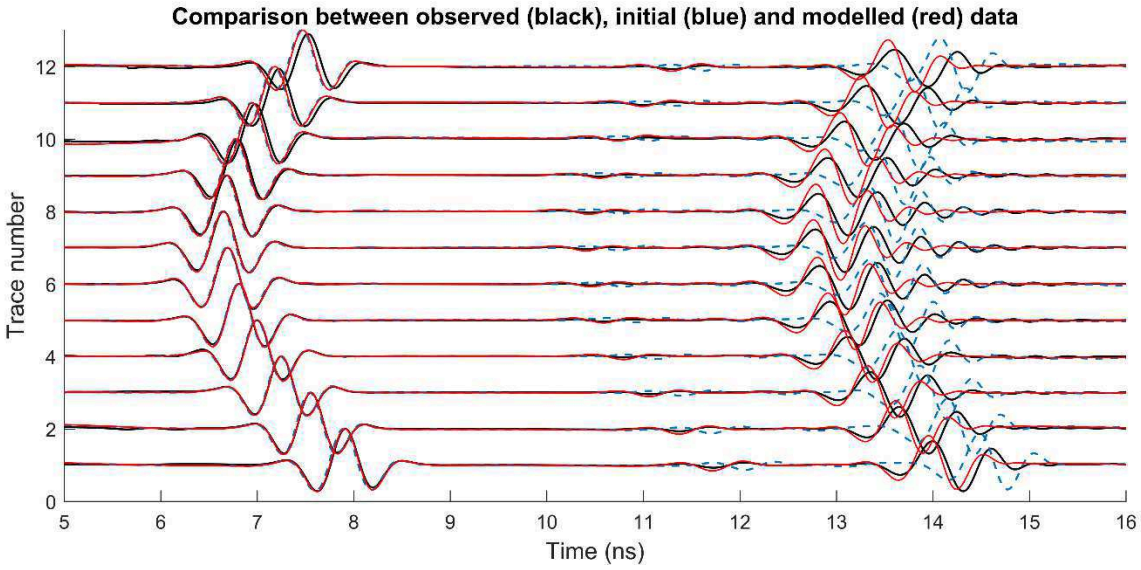

Figure 5. Comparison of observed "true" synthetic GPR traces (black), the GPR traces predicted from the initial model and corrected SW (blue) and the GPR traces predicted from the final inverted model (red). Traces are normalized individually.

The synthetic model results above show this FWI method is effective for improving estimates of pipe dimensions in highly idealized conditions. The effects of realistic soil

heterogeneities are missing. In the following section results of the method in real-world but well-controlled scenarios are presented.

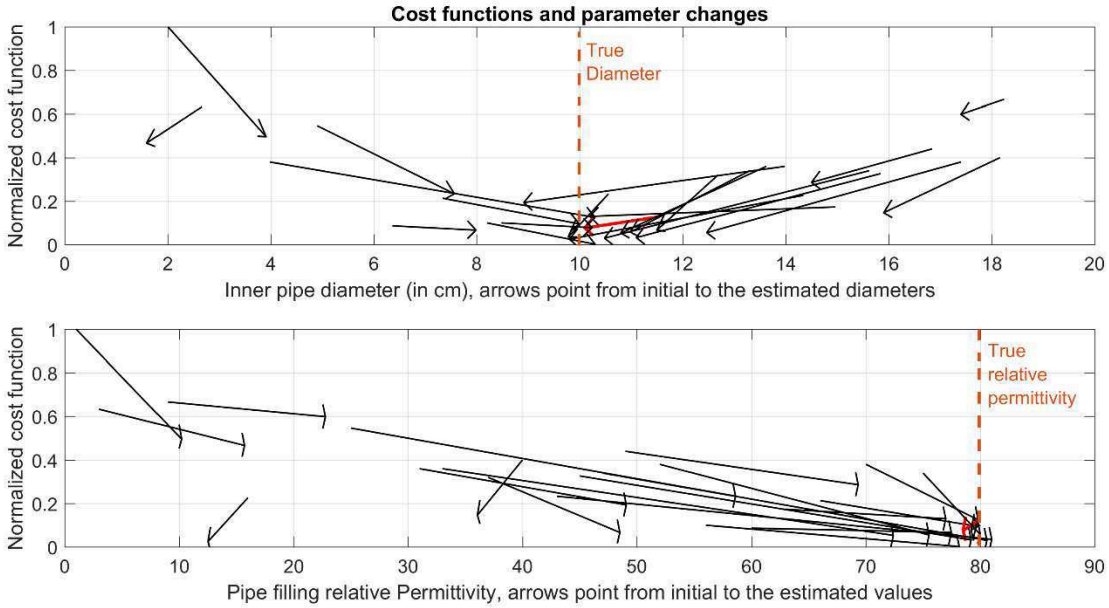

Figure 6. Cost function values associated with the initial guess (tail of arrow) and inversion output (tip of arrow) for 22 runs. Note in each run the initial values of the other variables in the inversion also vary. (Top) Cost function changes with inner pipe diameter. The dashed brown line marks the true (simulated) 10 cm pipe inner diameter. (Bottom) Cost function changes with infilling relative permittivity. The dashed brown line marks the true pipe filling relative permittivity of 80. With starting values of pipe diameter within a factor of two of the correct value, the inversion improves the estimate of the pipe diameter. Red arrows show the inversion run with starting parameters from the ray-based analysis, listed in Table 1.

Case studies of PVC pipe in well-sorted sands

The inversion method was tested with GPR profiles run across a buried PVC pipe of known position and dimensions. The field tests were run in the Geopark of the University of South Florida in Tampa, Florida, USA (http://hennarot.forest.usf.edu/main/depts/geosci/facilities/geopark.aspx). There, the uppermost 1-2 meters consist of well-sorted loose sand over progressively more silty and clay-rich layers (e.g. Bumpus and Kruse, 2014).

In mid-May 2016, a number of reconnaissance GPR profiles were collected to find an area with few tree roots and low degree of soil disturbance. Once a preferred location was found, a trench was excavated in order to bury a PVC pipe (Figure 7). The selected PVC pipe has an outer diameter of 8.2 cm and a wall thickness of 3 mm, and was placed so that the top of the pipe lay 35 cm below ground surface. One end of the horizontal PVC pipe was closed with a PVC lid and the other end was connected to another vertical pipe through a 90 degree PVC elbow. The 'L'-shaped pipe was designed to enable researchers to fill the pipe with liquids (Figure 7 Left and Middle; Figure 8). Once the burial depth of the top of the pipe was confirmed to be the same at the elbow location and the lid, the trench was refilled. Before refilling with the native sand, the sand was sieved to remove small tree roots. Attempts were made to make sure that the soil was as uniformly distributed as possible above the pipe to increase the chances of receiving clear diffracted hyperbolas.

Two subsequent GPR surveys were performed. The first was run on the empty, air-filled pipe on the same day the pipe was buried. The second was run almost 6 weeks later, in late July 2016. Although the soil was quite dry on the day of the July survey, there had been heavy rains in the 6 weeks since the pipe was installed, so it is assumed that the soil over the trench had settled and compacted to a degree more similar to undisturbed neighboring soil. For this second survey,

the pipe was completely filled with fresh water. In this paper, we discuss the July water-filled pipe survey first, because the data interpretation is more straightforward.

Figure 7. Left, the L-shaped PVC pipe in the hole in sand. Middle, the elbow part of the pipe showing the burial depth of 35 cm for the top of the horizontal part. Right, after filling the hole, the vertical part is visible that enables filling the pipe. The horizontal part of the pipe is aligned between the pink flags.

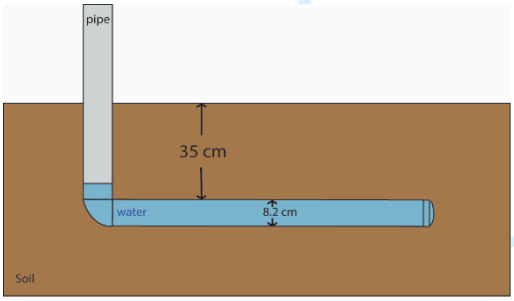

Figure 8. Schematic sketch of the pipe buried in sand. Blue color shows the water level in the pipe.

Case study 1, water-filled pipe

After the pipe was filled with water, as illustrated in Figure 8, a grid of 15 parallel profiles was acquired, with 5 cm spacing between profiles. (A subset is shown in Figure 9.) All profiles

were run in a north-south direction, perpendicular to the pipe which was laid in an east-west direction. A Mala-ProEx system with 800 MHz shielded antennas was used. The spacing between traces along each profile was set to 8.5 mm and was controlled by an odometer wheel, which was calibrated on site. The 80 traces centered on the hyperbola were selected to use in the inversion process. The water-filled pipe produces sharp hyperbolas in all the GPR profiles.

For a water-filled pipe, distinct reflections from both top and bottom of pipe are anticipated if the pipe diameter is greater than approximately half the radar wavelength. For this scenario a wavelength of about 4 cm is expected; the pipe diameter of 7.6 cm is almost twice this value. Clear hyperbolas are indeed observed from both top and bottom of the pipe in all 15 profiles. The central profile marked by the arrow in Figure 9 has one of the cleanest pipe returns recorded, and was selected for the full-waveform inversion.

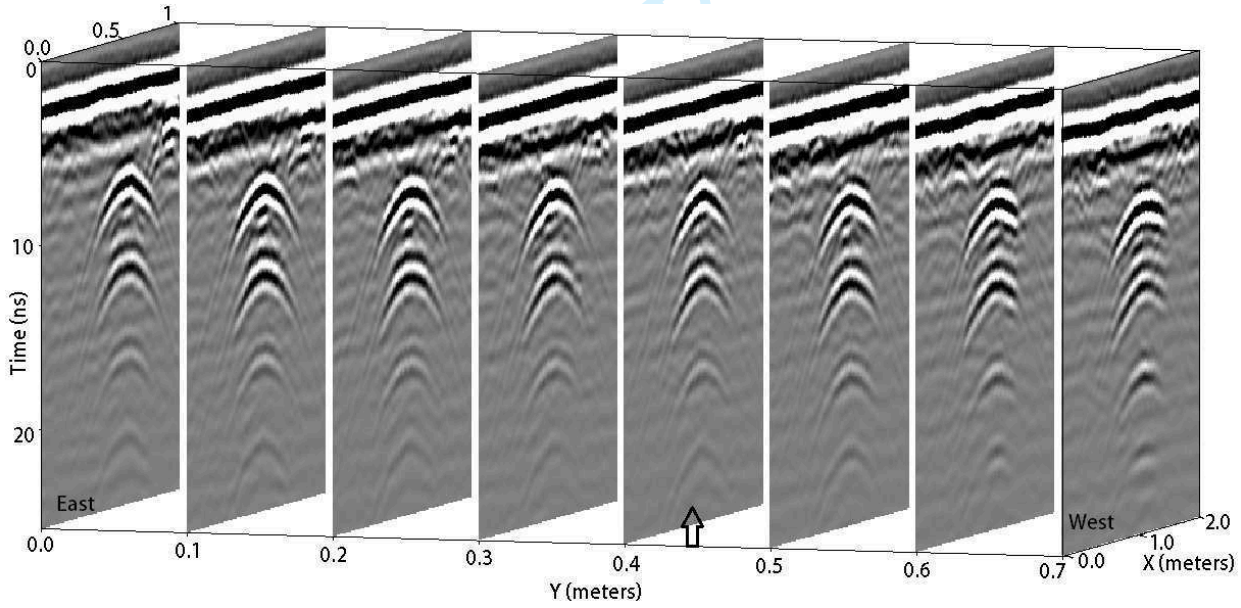

Figure 9. Profiles of the water-filled pipe buried in sand. The left-most left plot is closest to the pipe elbow; the right-most right closest to the lid. Diffracted hyperbolas are recorded from both

top and bottom of the pipe, at all locations. The arrow shows the profile used for full-waveform inversion.

From the selected profile, the closest 80 traces to the pipe were extracted for the FWI (Figure 9). The optimal data range and trace spacing for inversion is site-dependent, and beyond the scope of this paper. The ray-based analysis was performed on the selected data set (Table 2) followed by the 3D to 2D transformation. Figure 10 presents the 80 traces after basic filtering, including a 4 ns dewow filter, a time-zero correction, a high-cut 1600 MHz frequency filter, an average xy-filter with a 3×3 window size (this subjectively chosen window size smooths the data slightly, does not generally affect amplitudes on average by more than 1%, and improves the performance of the inversion process), and 3D to 2D transformation.

We found that the inversion procedure yields better results if the direct wave arrivals are excluded when computing the residuals vector *R* (Eq. 4). The direct arrivals are excluded as shown in Figure 10.

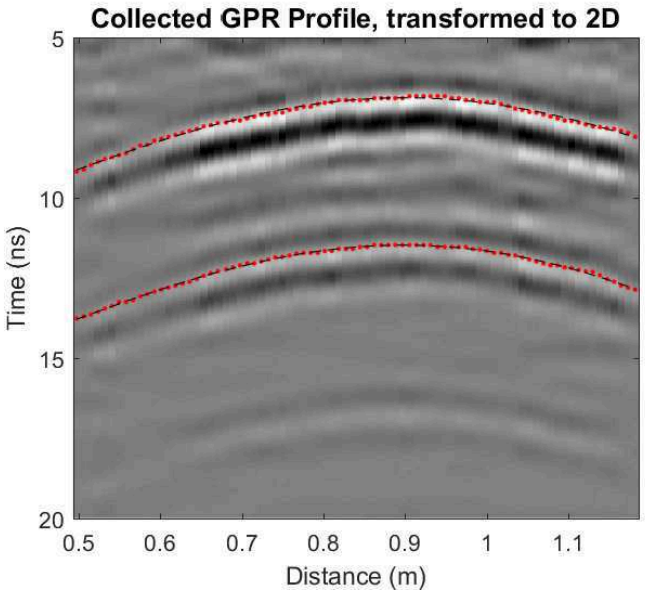

Figure 10. Profile over the water-filled pipe, direct wave excluded. The first strong return between 7-10 ns is the reflection from the top of the pipe, the second between 12-15 ns is from the bottom of the pipe. The latest weak return between 17-19 ns is a multiple. Red dots show the arrival time picks used in the ray-based inversion. Black dashed lines show the arrival time curves predicted form the ray-based inversion parameters.

The ray-based analysis was used to create an initial model to start the inversion. Since two diffraction hyperbolas are observed, we used the liquid-filled assumption for the pipe. Ray theory starting estimates are listed in Table 2. Conductivity values were fixed during FWI and traces were individually normalized in cost function calculations. Ray theory estimates the diameter with ~ 10% error if a good infilling permittivity is chosen (Table 2). The permittivity, conductivity and the wall thickness of the pipe itself (PVC) were assumed to be known and fixed to the actual values.

After setting the initial model parameters as described above, the initial synthetic GPR data were computed assuming a cell size of 1 mm x 1 mm in the gprMax 2D forward models and a 4th-derivative of the Gaussian wavelet as the SW. Using the deconvolution method, the SW was corrected twice (Figure 11). This wavelet is similar to that obtained for other data sets using a similar instrument from the same manufacturer (Klotzsche et al., 2013).

Neither the shape of the first reflected signals from the top of the pipe nor the second reflected signals from the bottom of the pipe are modelled acceptably with the initial guess parameters since the shape of the SW has not been corrected (see Figure 12 left). After the SW correction (Figure 12 middle), the reflections from the bottom of the pipe are still poorly fit because

the initial model still mis-estimates the pipe diameter. After 17 iterations the model and observed data fit is far superior (Figure 12 right).

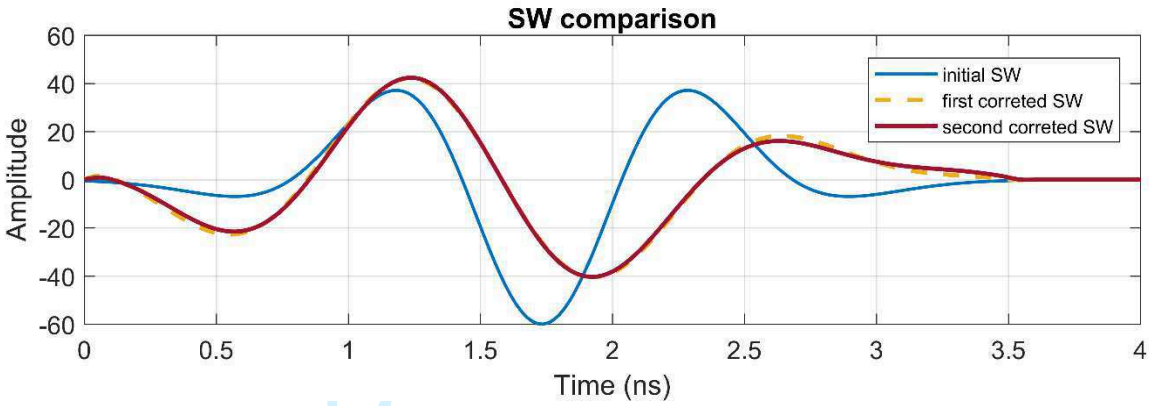

Figure 11. The initial and corrected effective source wavelets. The second corrected SW has an overall shape similar to the 4th Gaussian derivative but is not symmetric.

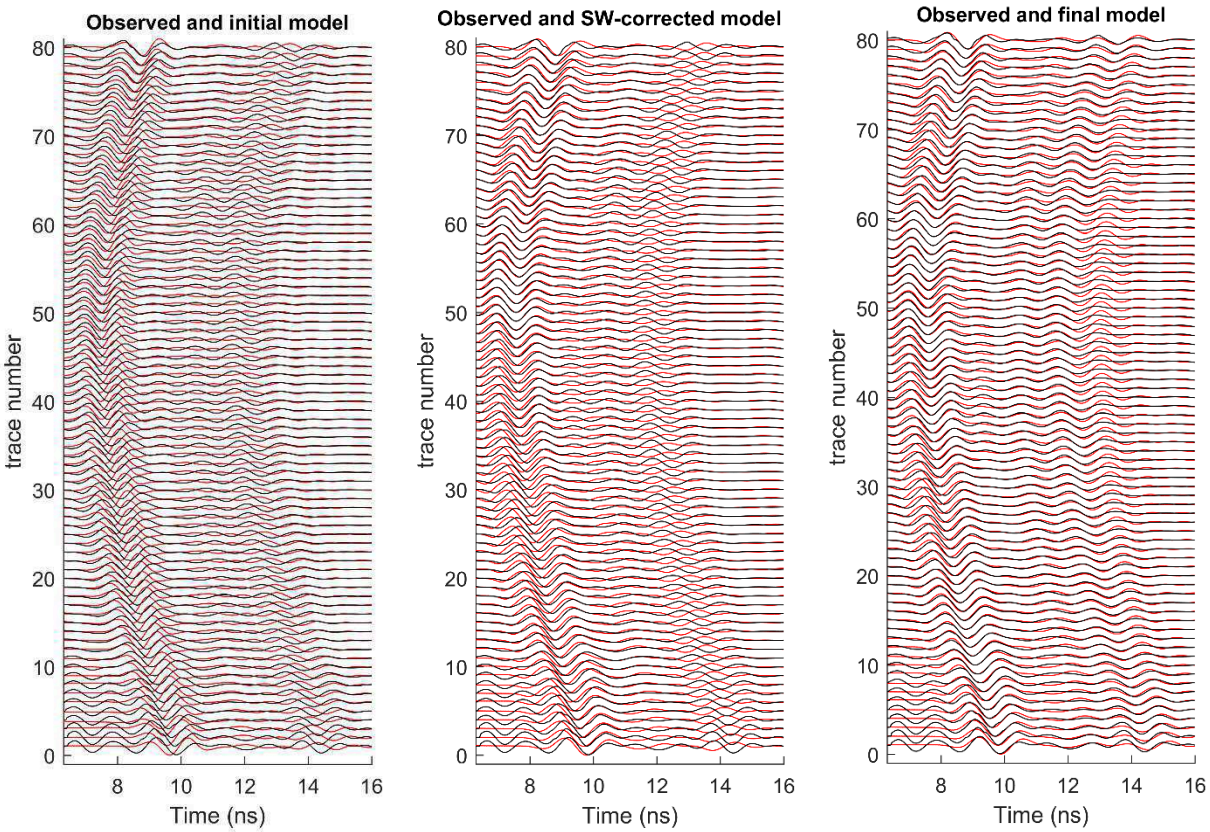

Figure 12. Left, observed data (black) and initial synthetic data (red) comparison. Middle, the same plot after the SW correction, first reflected signals fit better than the previous model. Right, same plot after the FWI process. A generally good fit between observed and modelled data is observed. Traces are normalized individually.

The inversion process maintains values for pipe-filling material that are close to the expected values for fresh water (see Table 2). The depth and pipe diameter are recovered to within 1% of their known values.

In order to investigate the sensitivity of the inversion algorithm to the initial values, the FWI process was run 20 times for the water-filled pipe case, similar to the process described above

for the synthetic model. Figure 13 summarizes the changes in cost function from the initial value to the final inversion value for the 20 runs, for pipe inner diameter (top) and pipe-filling relative permittivity (bottom).

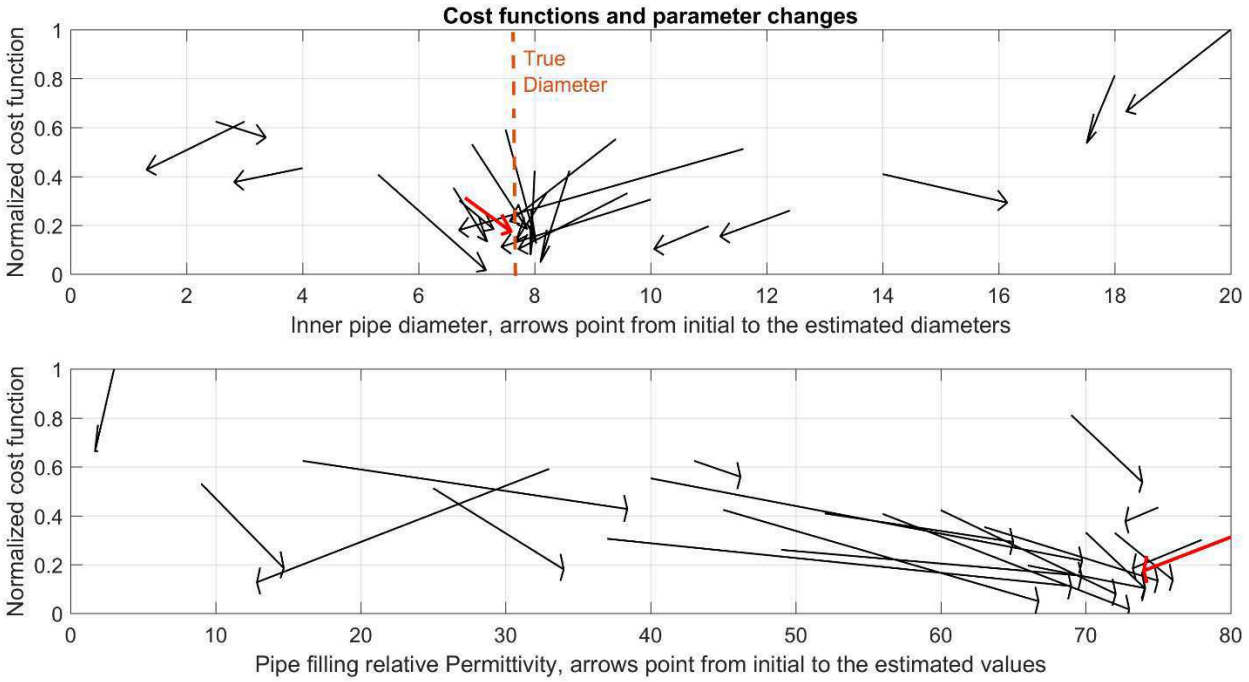

Figure 13. Cost function values associated with the initial guess (tail of arrow) and inversion output (tip of arrow) for 20 runs. Note in each run the initial values of the other variables in the inversion also vary. Red arrows belong to the inversion starting from ray-based analysis listed in Table 2. (Top) Cost function changes with inner pipe diameter. The dashed brown line marks the known 7.6 cm pipe inner diameter. With starting values of pipe diameter within 50% of the correct value, the inversion improves the estimate of the pipe diameter. (Bottom) Cost function changes with infilling relative permittivity.

Figure 13 illustrates that models with initial pipe diameters between 5 and 10 cm converge to within 1 cm of the 7.6 cm correct value. Models with more widely different starting values end up at local minima of the cost function.

Case study 2, air-filled pipe

On the same day that the pipe was buried, GPR profiles were collected using the 800 MHz antenna with the same settings as the previous section, but the pipe was empty. An air-filled pipe should produce both weaker reflections and a shorter time gap between upper and lower returns. Presumably also the sand covering the pipe was less uniformly compacted and drier on the day of burial than 6 weeks later, and thus we expect both more "background noise" and a longer incoming wavelength in this case. These factors combine to make the FWI in this case more challenging, designed to illustrate e the efficiency of this technique in a more complex case.

A GPR profile (Figure 14) was selected for the inversion procedure at the same location of the inverted profile in case study 1. Comparing Figures 14 and 10 illustrates the expected effects of water vs. air and of soil compaction. The air-filled pipe produces less pronounced and overlapping diffraction hyperbolas. There is also some scattered energy recorded before the hyperbolas, as anticipated due to heterogeneity in the sand. Using the ray-based scheme, the average sand relative permittivity was estimated to be 4.52, i.e. an average velocity of almost 0.14 m/ns, indicating the sand was much dryer at the time of this survey than at the time of the later survey over the water-filled pipe. The depth and the lateral location of the pipe are well estimated from the ray-based analysis (Table 2). Since there is just one hyperbola recorded from the pipe,

the diameter and pipe-filling conductivity estimation are challenging. Traditional hyperbola fitting anticipates the pipes within diameter of 3-30 cm to be a fit to this data. Since start model parameters should be provided for FWI, the initial diameter of the pipe is set to 12 cm for the sample run. We can guess that the pipe is filled with air, and appropriate permittivity and conductivities are assigned.

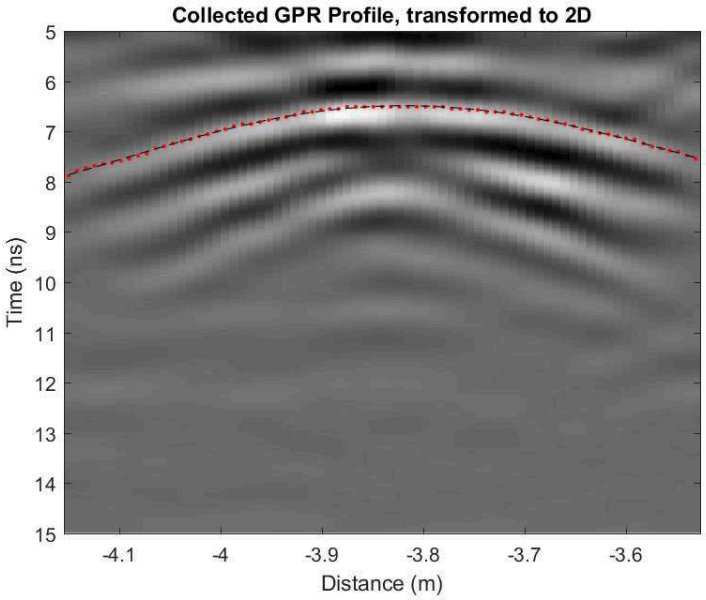

Figure 14. GPR profile over the air-filled pipe, direct wave excluded. A primary reflection from the top of the pipe is observed between 6-9 ns. Dewow, zero-time correction, band-pass and average xy-filters are applied with the same settings as for the water-filled pipe (Figure 10). Data are transformed to 2D. Red dots show the arrival time picks used in the ray-based inversion. Black dashed lines show the arrival time curves predicted form the ray-based inversion parameters.

The 3D to 2D transformation, effective SW estimation (Figure 15) and inversion procedure and assumptions are identical to those described for the water-filled pipe. Similar to two previous cases, the unknowns assigned to the inversion procedure are pipe position, pipe diameter and soil and pipe-filling permittivities. Initial parameter values for a sample run are listed in Table 2; the inversion results are presented in Figure 16.

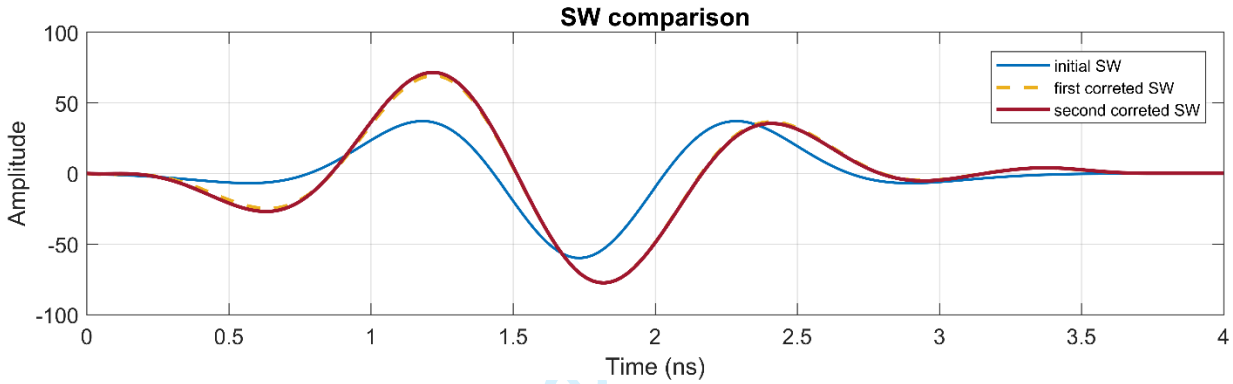

Figure 15. The initial and corrected effective source wavelets for the air-filled pipe.

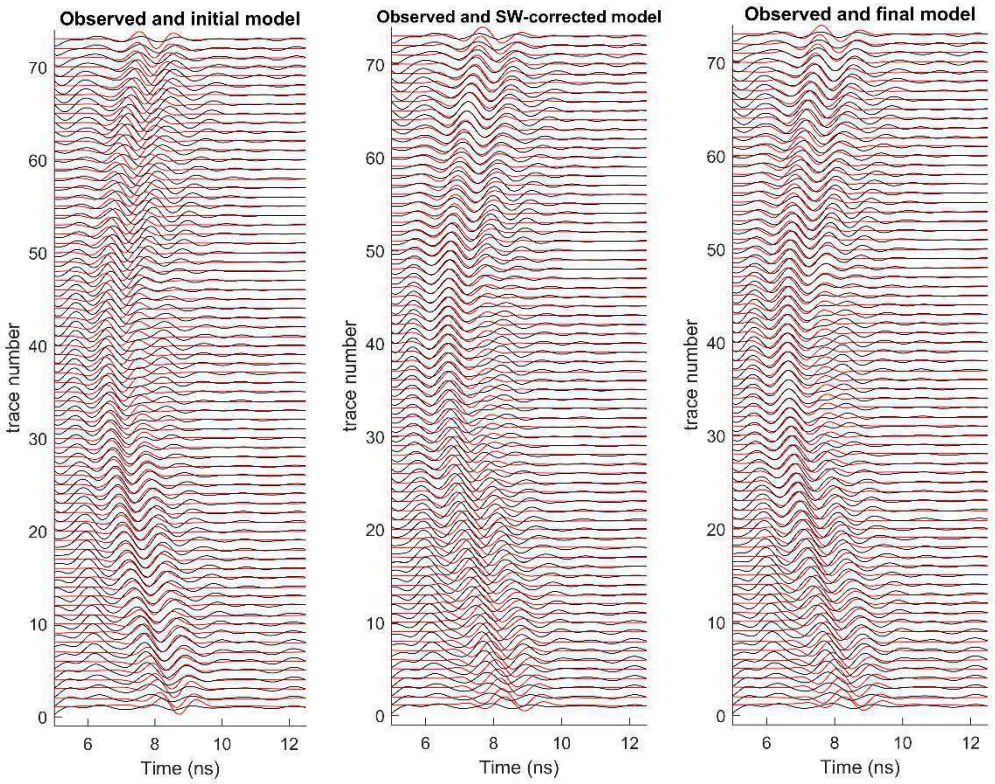

Figure 16. Left, observed data (black) and initial synthetic data (red) comparison. Middle, The same plot after the SW correction. The reflected signals are better fit. Right, same plot after the FWI process.

The final model after the FWI is an improved but clearly imperfect fit to the real data, with the inverted parameter values listed in Table 2. Misfits are presumably caused in part by unmodeled soil heterogeneities. The pipe dimension is recovered with 8% error.

In order to investigate the quality of inversion results and assess local minima of the cost function, 20 different models were run with different starting parameters (permittivity of pipe filling and diameter and depth). The SW was estimated for each of the tests separately. Figure 17 summarizes the changes in cost function from the initial value to the final inversion value for the 20 runs, for pipe inner diameter (top) and pipe-filling relative permittivity (bottom).

Because of the interference (overlap) in returns between the top of the pipe and the bottom of the pipe in the air-filled case, models that started with initial diameters significantly too large or too small fail to account for the overlap and yield source wavelets that look dramatically different from those of the better models. This in turn yields unsatisfactory inversion results, underscoring the importance of the initial model. These tests for the air-filled case suggest initial models with diameters within 30% of the true diameter are consistently improved in the inversion process.

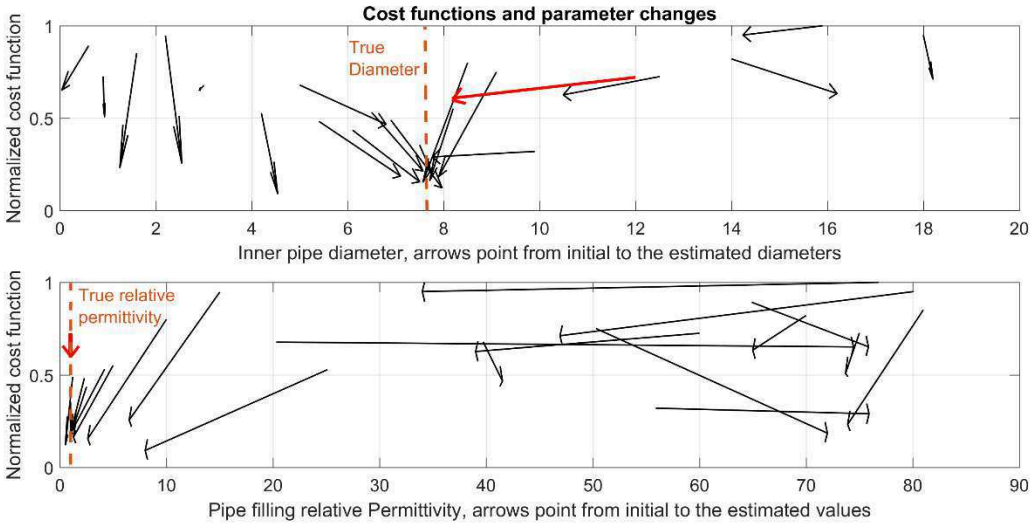

Figure 17. Cost function values associated with the initial guess (tail of arrow) and inversion output (tip of arrow) for 20 runs. Red arrows belong to the inversion included in Table 2. (Top) Cost function changes with inner pipe diameter. The dashed brown line marks the known 7.6 cm pipe inner diameter. (Bottom) Cost function changes with infilling relative permittivity. The dashed brown line marks 1 as the relative permittivity of air. The inversion process clearly targets local minima if the initial estimate of pipe-filling permittivity is poor.

Table 2, here

DISCUSSION

In these simple field tests, the pipe diameter estimates are significantly improved when the initial guess is within ~50% of the true value for the water-filled pipe with distinct returns from top and bottom, and within ~30% of the true value for the air-filled pipe. With the good initial guess, inversion generally proceeds to within 1 cm or less of the true value (in this case to <8% error). This is an improvement over the traditional ray-based scheme, in which the diameter is estimated by trial-and-error fit of the observed hyperbola to the expected arrival times for returns over pipes of varying sizes. As described in the introduction, the trial-and-error fit for the air-filled pipe case (inner diameter 7.6 cm) yielded reasonable results for diameters ranging from 3 to 30 cm.

This method in its current form is thus suitable for improving good starting estimates of pipe diameter in simple cases with isolated diffraction hyperbolas. Examination of model runs such as those shown in Tables 1 and 2 and Figure 13 shows that the initially good pipe diameter estimates are also typically slightly improved in the inversion. Conductivity values are fixed to the ray-based analysis results, for the reasons described for previous cases above. To obtain conductivities, the SW could be updated during the FWI following a process similar to Busch et al. (2012; 2014).

The method described here shares the conclusions of Meles et al. (2012) that starting model estimates must be sufficiently good that synthetic data pulses are offset less than one-half wavelength from the measured traces. For the clean synthetic data, this criteria can be met with a model that assumes a permittivity within 50% of the correct value, and the inversion proceeds

toward a permittivity closer to the correct value. For the field data case where two diffracted hyperbolas are recorded ray theory can provide a good starting model parameters for the FWI process. In cases of gas-filled pipes (or very narrow liquid-filled cylinders, such as tree roots) that are likely to generate just one diffraction hyperbola, the ray theory fails to provide good starting models, in this case the best judgment of the user must be used to set the initial model parameters. In this sense, a successful inversion confirms the initial guess, while a failure to converge or a small reduction in cost function suggests a poor starting model.

CONCLUSIONS

This paper introduces a new method for FWI of common-offset GPR data, particularly targeting the dimensions and infilling material of buried pipes. The method is designed to be used where clear isolated diffraction hyperbolas indicate the presence of a pipe, but pipe dimensions and filling may be unknown. The method consists of five main steps: GPR data processing, ray-based analysis to set a good initial model, 3D to 2D transformation of data, effective SW estimation, and full-waveform inversion. The method combines two freely available software packages: PEST, for the inversion, and gprMax for forward modeling of the GPR data.

This method is applied on a synthetic 3D dataset and two 800 MHz GPR profiles collected over a PVC pipe buried in clean sands. In the synthetic and water-filled and air-filled pipe field cases, good initial estimates of the depth and diameter of the pipe from the ray-based analysis are improved after FWI. The tests show that while the initial estimate of pipe diameter is within 30-50% of the true value, the inversion yields estimates with <8% error. For the field data, the requirement of a good starting model can in practice confirm or deny a starting assumption about the pipe-filling material.

Ray-based analysis is essential to set up the starting model, particularly to estimate the pipe location and average soil permittivity and conductivity. Although ray-based conductivity estimates are possible, improvement in the conductivity would require the SW to be updated after each iteration in the FWI procedure. Iterations on the SW during the FWI process, as in Busch et al. (2012; 2014), are beyond the scope of this study.

The method in its present form is only effective for isolated hyperbolas, and assumes that GPR surveys are conducted with broadside antenna geometry along profiles perpendicular to horizontal pipes. Furthermore, the soil is assumed to be locally homogenous. Relaxation of these conditions is the subject of ongoing research.

ACKNOWLEDGEMENTS

The authors are very grateful to Jan van der Kruk for very constructive comments, Sanaz Esmaeili and Christine Downs for field assistance, Denis Voytenko and Nicholas Voss for their introduction to PEST, Antonis Giannopoulos and Craig Warren for their help with gprMax, and Anthony Green for assistance implementing algorithms on the USF Research Computing cluster. Sebastian Busch, George Tsoflias, Blair Schneider and three anonymous reviewers gave productive reviews that greatly improved the manuscript.

Appendix A

Assuming homogeneous soil, the amplitude of the GPR wave decays due to geometric spreading and soil attenuation. The combination of these two effects can be described with wave

amplitude proportional to $e^{-\alpha r}/r$ in 3D media, in which the attenuation term α can be described as

$$\alpha = \frac{\sigma}{2}\sqrt{\frac{\mu}{\varepsilon}} \quad \text{Equation A-1}$$

where σ is the soil conductivity, μ magnetic permeability, and ε the mean absolute electrical permittivity of the soil.

To estimate the conductivity of the soil, the peak amplitudes of the first pipe diffraction hyperbola arrivals are picked and used in a least squares inversion for the attenuation term, and thereby the soil conductivity. Assuming far-field amplitudes, a uniform antenna radiation pattern, and a uniform reflection coefficient from all parts of the pipe, the amplitude A of the wave having traveled a distance r is expressed as:

$$A = A_0 \frac{e^{-\alpha r}}{r} \quad \text{Equation A-2}$$

where A_0 is a constant. The term $e^{\alpha r}$ can be replaced the first two terms of its Taylor series expansion, $1 + \alpha r$, leaving $A = A_0 \frac{1}{(e^{\alpha r})r} \approx A_0 \frac{1}{(1+\alpha r)r}$. Rearranging,

$$\left(\frac{1}{A_0}\right)Ar + \left(\frac{\alpha}{A_0}\right)Ar^2 = 1 \quad \text{Equation A-3}$$

By picking the peak amplitude and computing the travel distance for each trace in the diffraction hyperbola, the Jacobian matrix J is created. Then the unity vector I and parameter vector P are calculated via:

$$J = \begin{bmatrix} A_1 r_1 & A_1 r_1^2 \\ A_2 r_2 & A_2 r_2^2 \\ \vdots & \vdots \\ A_n r_n & A_n r_n^2 \end{bmatrix}; P = \begin{bmatrix} p_1 \\ p_2 \end{bmatrix}; I = \begin{bmatrix} 1 \\ 1 \\ \vdots \\ 1 \end{bmatrix} \quad \text{Equation A-4}$$

The parameter vector P can be estimated with the least squares solution ($P = (J^T J)^{-1} J^T I$) of these systems using equation A-4. The attenuation term α is estimated as:

$$\alpha = \frac{p_2}{p_1} \quad \text{Equation A-5}$$

We note the simplifying assumptions about far-field amplitudes, radiation patterns, and uniform scattering are not strictly valid in real scenarios. However, tests showed that more complicated models did not yield conductivity estimates that consistently produced better inversion results.

REFERENCES

André, F., Jonard M., Lambot, S., 2015, Non-Invasive Forest Litter Characterization Using Full-Wave Inversion of Microwave Radar Data, IEEE Transactions on Geoscience and Remote Sensing, vol. 53, no. 2, pp. 828-840, doi: 10.1109/TGRS.2014.2328776

Benedetto, A., Pajewski L., 2015, Civil engineering applications of Ground Penetrating Radar, Springer Transactions in Civil and Environmental Engineering.

Booth, A., Clark, R. A., Murray, T., 2011, Influences on the resolution of GPR velocity analyses and a Monte Carlo simulation for establishing velocity precision, Near Surface Geophysics, 9, 399-411, doi:10.3997/1873-0604.2011019.

Bumpus, P. B., Kruse, S., 2014, Case History Self-potential monitoring for hydrologic investigations in urban covered-karst terrain, Geophysics. 79, No. 6, B231–B242.

Busch, S., van der Kruk, J., Bikowski, J., Vereecken, H., 2012, Quantitative conductivity and permittivity estimation using full-waveform inversion of on- ground GPR data, Geophysics, 77, H79-H91, doi:10.1190/GEO2012-0045.1.

Busch, S., van der Kruk, J., Vereecken, H., 2014, Improved characterization of fine-texture soils using on-ground GPR full-waveform inversion, IEEE Transactions On Geoscience And Remote Sensing, 52 No. 7, 3947-3958, doi: 10.1109/TGRS.2013.2278297.

Crocco, L., Prisco, G., Soldoveiri, F., Cassidy, N. J., 2009, Early-stage leaking pipes GPR monitoring via microwave tomographic inversion, Journal of Applied Geophysics, 67, 270-277.

De Coster, A., Tran, A. P., Lambot, S., 2016, Fundamental Analyses on Layered Media Reconstruction Using GPR and Full-Wave Inversion in Near-Field Conditions, IEEE Transactions on Geoscience and Remote Sensing, vol. 54, no. 9, pp. 5143-5158, doi: 10.1109/TGRS.2016.2556862

Demirci S., Yigit E., Eskidemir I. H., Ozdemir C., 2012, Ground penetrating radar imaging of water leaks from buried pipes based on back-projection method, NDT&E International, 47, 35-42.

Doherty, J., 2010, PEST Model-Independent Parameter Estimation User Manual: 5th Edition, Watermark Numerical Computing.

Doherty, J., 2015, Calibration and Uncertainty Analysis for Complex Environmental Models, PEST: complete theory and what it means for modelling the real world, Watermark Numerical Computing.

Doherty, J., 2017, PEST, http://www.pesthomepage.org/.

Ernst, J. R., Green, A. G., Maurer, H., Holliger, K., 2007, Application of a new 2D time-domain full-waveform inversion scheme to crosshole radar data, GEOPHYSICS. 72, No. 5, J53–J64.

Dou Q., Wei, L., Magee D. R., Cohn A. G., 2017, Real-Time Hyperbola Recognition and Fitting in GPR Data, IEEE Transactions on Geoscience and Remote Sensing, vol. 55, no. 1, pp. 51-62.

Fisher, S. C., Stewart, R. R., Jol, H. M., 1992, Processing ground penetrating radar (GPR) data, CREWES Research Report, Volume 4, 11-2 – 11-22.

Forbriger, T., Groos, L., Schafer,M., 2014, Line-source simulation for shallow-seismic data. Part 1: theoretical background, Geophysical Journal International, 198, 1387–1404, doi: 10.1093/gji/ggu199.

Giannopoulos, A., 2005, Modelling ground penetrating radar by GprMax, Construction and Building Materials, 19(10), 755-762, doi: 10.1016/j.conbuildmat.2005.06.007

Grandjean, G., Gourry, J. C., Bitri, A., 2000, Evaluation of GPR techniques for civil-engineering applications: study on a test site, Journal of Applied Geophysics 45, 141–156.

Gueting, N., Klotzsche, A., van der Kruk, J., Vanderborght, J., Vereecken, H., Englert, A., 2015, Imaging and characterization of facies heterogeneity in an alluvial aquifer using GPR full-waveform inversion and cone penetration tests, Journal of Hydrology, Volume 524, Pages 680-695, ISSN 0022-1694, doi: 10.1016/j.jhydrol.2015.03.030.

Gueting, N., Vienken, T., Klotzsche, A., van der Kruk, J., Vanderborght, J., Caers, J., Vereecken, H., and Englert, A., 2017, High resolution aquifer characterization using crosshole GPR full-waveform tomography: Comparison with direct-push and tracer test data, Water Resources Research, 53, 49–72, doi:10.1002/2016WR019498.

Janning, R., Busche, A., Horvath, T., Schmidt-Thieme, L., 2014, Buried pipe localization using an iterative geometric clustering on GPR data, Artif Intell Rev, 42, 403–425; doi: 10.1007/s10462-013-9410-2.

Jazayeri, S., Kruse, S., 2016, Full-waveform inversion of ground-penetrating radar (GPR) data using pest (FWI-pest method) applied to utility detection, SEG Technical Program Expanded Abstracts 2016, 2474-2478, doi: 10.1190/segam2016-13878165.1

Kalogeropoulos, A., van der Kruk, J., Hugenschmidt, J., Busch, S., Merz, K., 2011, Chlorides and moisture assessment in concrete by GPR full waveform inversion, Near Surface Geophysics, 9, 277-285, doi:10.3997/1873-0604.2010064.

Keskinen, J., Klotzsche, A., Looms, M. C., Moreau, J., van der Kruk, J., Holliger, K., Stemmerik, L., Nielsen, L., 2017, Full-waveform inversion of Crosshole GPR data: Implications for porosity estimation in chalk, Journal of Applied Geophysics, Volume 140, Pages 102-116, doi: 10.1016/j.jappgeo.2017.01.001.

Klotzsche, A., van der Kruk, J., Bradford, J., Vereecken, H., 2014, Detection of spatially limited high-porosity layers using crosshole GPR signal analysis and full-waveform inversion, Water Resources Research 50, doi: 10.1002/2013WR015177.

Klotzsche, A., van der Kruk, J., Linde, N., Doetsch, J. A., Vereecken, H., 2013, 3-D characterization of high-permeability zones in a gravel aquifer using 2-D crosshole GPR full-waveform inversion and waveguide detection, Geophysical Journal International, 195, 932-944, doi: 10.1093/gji/ggt275.

Klotzsche, A., van der Kruk, J., Meles, G. A., Doetsch, J. A., Maurer, H., Linde, N., 2010, Full-waveform Inversion of Crosshole Ground Penetrating radar Data to Characterize a Gravel Aquifer close to the Thur River, Switzerland, Near Surface Geophysics, 8, 631-646, doi: 10.3997/1873-0604.2010054.

Klotzsche, A., van der Kruk, J., Meles, G., Vereecken, H., 2012, Crosshole GPR full-waveform inversion of waveguides acting as preferential flow paths within aquifer systems, Geophysics, 77(4), H57-H62, doi: 10.1190/geo2011-0458.1.

Lambot, S., Slob, E. C., van den Bosch, I., Stockbroeckx, B., Vanclooster, M., 2004, Modeling of ground-penetrating Radar for accurate characterization of subsurface electric properties, IEEE Transactions on Geoscience and Remote Sensing, vol. 42, no. 11, pp. 2555-2568, doi: 10.1109/TGRS.2004.834800.

Lavoué, F., Brossier, R., Métivier, L., Garambois, S., Virieux, J., 2014, Two-dimensional permittivity and conductivity imaging by full waveform inversion of multioffset GPR data: a frequency-domain quasi-Newton approach, Geophysical Journal International, Volume 197, Issue 1, Pages 248–268, doi: 10.1093/gji/ggt528

Lester, J., Bernold, L. E., 2007, Innovative process to characterize buried utilities using Ground Penetrating Radar, Automation in Construction, 16, 546-555; doi:10.1016/j.autcon.2006.09.004.

Liu, H., and M. Sato (2014), In situ measurement of pavement thickness and dielectric permittivity by GPR using an antenna array, NDT E Int., 64(June), 65–71, doi:10.1016/j.ndteint.2014.03.001.

Liu, H., X. Xie, K. Takahashi, and M. Sato (2014), Groundwater Level Monitoring for Hydraulic Characterization of an Unconfined Aquifer by Common Mid-point Measurements using GPR, JEEG,19(4), 259–268, doi:10.2113/JEEG19.4.xx.

Loeffler, O., Bano, M., 2004, Ground Penetrating Radar Measurements in a Controlled Vadose Zone: Influence of the Water Content, Vadose Zone Journal 3:1082–1092

Mahmoudzadeh Ardakani, M. R., Jacques D. C., Lambot, S., 2016, A Layered Vegetation Model for GPR Full-Wave Inversion, IEEE Journal of Selected Topics in Applied Earth Observations and Remote Sensing, vol. 9, no. 1, pp. 18-28, doi: 10.1109/JSTARS.2015.2418093

Maierhofer, C., Reinhardt, H., Dobmann, G., 2010, Non-Destructive Evaluation of Reinforced Concrete Structures, Volume 1: Deterioration processes and standard test methods, 1st Edition, Woodhead publishing limited.

Meles, G. A., Van der Kruk, J., Greenhalgh, S. A., Ernst, J. R., Maurer, H., Green, A. G., 2010, A new vector waveform inversion algorithm for simultaneous updating of conductivity and permittivity parameters from combination crosshole/borehole-to-surface GPR data, IEEE

Transactions on Geosciences and Remote Sensing, Vol. 48, Issue 9, pp. 3391-3407, doi: 10.1109/TGRS.2010.2046670.

Meles, G. A., Greenhalgh, S. A., Van der Kruk, J., Green, A. G., Maurer, H., 2012, Taming the non-linearity problem in GPR full-waveform inversion for high contrast media, Journal of Applied Geophysics, Volume 78, Pages 31-43, doi: 10.1016/j.jappgeo.2011.12.001

Murray, T., Booth, A., Rippin D. M., 2007, Water-Content of Glacier-Ice: Limitations on Estimates from Velocity Analysis of Surface Ground-Penetrating Radar Surveys, JEEG, Volume 12, Issue 1, 87–99.

Ni, S., Huang Y., Lo K., Lin D., 2010, Buried pipe detection by ground penetrating radar using the discrete wavelet transform, Computers and Geotechnics, 37, 440-448.

Radzevicius, S., 2015, Least-Squares Curve Fitting for Velocity and Time Zero, Proc. 8th IWAGPR, pp. 1-4.

Ristic A. V., Petrovacki D., Govedarica M., 2009, A new method to simultaneously estimate the radius of a cylindrical object and the wave propagation velocity from GPR data, Computers & Geosciences 35, 1620–1630.

Roberts R. L., Daniels, J. J., 1996, Analysis of GPR Polarization Phenomena, JEEG, Volume 1, Issue 2, 139-157.

Sham, J. F. C., Lai, W. W. L., 2016, Development of a new algorithm for accurate estimation of GPR's wave propagation velocity by common-offset survey method, NDT&E International, 83, 104–113.

Tran, A. P., André, F., Lambot, S., 2014, Validation of Near-Field Ground-Penetrating Radar Modeling Using Full-Wave Inversion for Soil Moisture Estimation, IEEE Transactions on Geoscience and Remote Sensing, vol. 52, no. 9, pp. 5483-5497, doi: 10.1109/TGRS.2013.2289952

van der Kruk, J., Gueting, N., Klotzsche, A., He, G., Rudolph, S., von Hebel, C., Yang, X., Weihermüller, L., Mester, A., Vereecken, H., 2015, Quantitative multi-layer electromagnetic induction inversion and full-waveform inversion of crosshole ground penetrating radar data, Journal of Earth Science, Volume 26, Issue 6, pp 844-850, doi: 10.1007/s12583-015-0610-3

Villela, A., and J.M. Romo, 2013, Invariant properties and rotation transformations of the GPR scattering matrix: Journal of Applied Geophysics, 90, 71-81.

Warren, C., Giannopoulos, A., Giannakis, I., 2016, gprMax: Open source software to simulate electromagnetic wave propagation for Ground Penetrating Radar, Computer Physics Communications, 209, 163-170, doi: 10.1016/j.cpc.2016.08.020.

Yang, X., Klotzsche, A., Meles, G., Vereecken, H., van der Kruk, J., 2013, Improvements in crosshole GPR full-waveform inversion and application on data measured at the Boise Hydrogeophysics Research Site, Journal of Applied Geophysics, Volume 99, Pages 114-124, doi: 10.1016/j.jappgeo.2013.08.007.

Zeng, X., McMechan, G., 1997, GPR characterization of buried tanks and pipes, Geophysics, Vol. 62, No. 3.

LIST OF FIGURES

Figure 14. GPR profile over the air-filled pipe, to be taken in FWI, direct wave excluded.

Figure 15. The initial and corrected SWs for real data, air-filled pipe.

Figure 16. Comparison between observed, initial and inverted data for air-filled pipe.

Figure 17. Cost function values associated with the initial guess and inversion output for 20 runs, air-filled pipe.

LIST OF TABLES

Table 1. The correct, initial guess, and inverted parameter values for the synthetic model. Pipe diameter and pipe-filling material permittivity estimates are significantly improved by the inversion process.

Parameter		Correct value	Ray-based estimation	FWI result with the ray-based results as the starting model	Estimation Error (%)
Synthetic model of Water-filled pipe	Relative Permittivity of Soil	5	5.1	5.09	1.8
	Electrical conductivity of soil (mS/m) (Fixed)	2	2.3	--	--
	Relative Permittivity of pipe-filling material (water)	80	80	78.5	2.25
	Electrical conductivity of pipe-filling material (water) (mS/m)	1	2.5	--	--
	X (center of the pipe) (cm)	50	49.95	49.95	0.1
	Depth of top of the pipe (cm)	35	33.65	35.08	0.23
	Pipe wall thickness (mm) (Fixed)	3	--	--	--
	Pipe inner diameter (cm)	10	11.5	10.12	1.2
	Pipe relative permittivity (PVC) (Fixed)	3	--	--	--
	Pipe electrical conductivity (mS/m) (PVC) (Fixed)	10	--	--	--

Table 2. Sample inversion results for both air and water filled pipes. Ray-based analysis results are used as the initial values in the FWI. Soil conductivity and pipe-filling conductivity are fixed to the ray-based results during FWI.

Parameter		Correct value	Ray-based estimation	FWI result with the ray-based results as the starting model	Estimation Error (%)
Water filled pipe	Relative Permittivity of Soil	--	5.822	5.85	--
	Electrical conductivity of soil (mS/m) (Fixed)	--	3.2	--	--
	X (center of the pipe) (m)	1.09	1.088	1.09	0
	Depth of top of the pipe (cm)	35	33.55	34.84	0.46
	Pipe wall thickness (mm) (Fixed)	3	--	--	--
	Pipe inner diameter (cm)	7.6	6.86.8	7.59	0.13
	Relative Permittivity of pipe-filling material (water)	--	80	74	--
	Effective electrical conductivity of pipe-filling material (water) (mS/m) (Fixed)	--	0.02	--	--
	Pipe relative permittivity (PVC) (Fixed)	--	3	--	--
	Pipe electrical conductivity (mS/m) (PVC) (Fixed)	--	1	--	--
Air-filled pipe	Relative Permittivity of Soil	--	4.52	4.6	--
	Electrical conductivity of soil (mS/m) (Fixed)	--	4.23	--	--
	X (center of the pipe)	1.09	1.095	1.092	0.18
	Depth of top of the pipe (cm)	35	34.7	34.8	0.57
	Pipe wall thickness (mm) (Fixed)	3	--	--	--
	Pipe inner diameter (cm)	7.6	Between 3 and 30	8.18 (start value 12)	7.6
	Relative Permittivity of pipe-filling material (air)	1	1	1	0
	Effective electrical conductivity of pipe-filling material (air) (mS/m) (Fixed)	0	--	--	--
	Pipe relative permittivity (PVC) (Fixed)	--	3	--	--
	Pipe electrical conductivity (mS/m) (PVC) (Fixed)	--	1	--	--